Spectrochimica Acta Part B: Atomic Spectroscopy 237 (2026) 107449

Contents lists available at ScienceDirect

Spectrochimica Acta Part B: Atomic Spectroscopy

journal homepage: www.elsevier.com/locate/sab

Evaluating analytical methods for ancient glass: Validation of micro-XRF quantitative data through comparison with LA-ICP-MS

Sabrina Molinaro [a,b], Roberta Zanini [a], Kalliopi Tsampa [c], Elti Cattaruzza [b], Andreas G. Karydas [c,*], Arianna Traviglia [a,*]

[a] Istituto Italiano di Tecnologia-Center for Cultural Heritage Technology, via Adriano Olivetti, 1, 31056 Roncade (TV), Italy
[b] Department of Molecular Sciences and Nanosystems, Ca' Foscari University of Venice, via Torino, 155, 30172 Venice, Italy
[c] Institute of Nuclear and Particle Physics, NCSR "Demokritos", Agia Paraskevi, 15341 Athens, Greece

ARTICLE INFO

Keywords:
μ-XRF
LA-ICP-MS
Ancient glass
Quantitative analysis
Reproducibility

ABSTRACT

This study aims to assess the reliability of micro-X-ray fluorescence spectroscopy (μ-XRF) as a quantitative, non-invasive tool for the *in-situ* compositional analysis of ancient glass. μ-XRF is widely employed in archaeological and materials science contexts due to its ability to rapidly detect major, minor, and trace elements without the need for sampling. However, it is often assumed that its limited sensitivity to light elements ($Z < 13$) in field applications poses challenges for a comprehensive characterisation of glass-making technologies and raw materials. In this study, we evaluate the analytical performance of μ-XRF for glass analysis, going beyond compositional characterisation by systematically comparing it with Laser Ablation Inductively Coupled Plasma Mass Spectrometry (LA-ICP-MS). LA-ICP-MS offers superior detection limits and a broader elemental range, but its use is constrained by the need for sample preparation and its non-portable nature. The precision of μ-XRF was assessed through repeated daily measurements, while accuracy was evaluated using the certified reference glasses Corning A and B. Correction trends were developed by comparing μ-XRF results with both the nominal concentrations of these standards and with corresponding LA-ICP-MS data, in order to mitigate inherent limitations and enhance the method's reliability. The validated protocol was then applied to a set of Roman glass samples of unknown composition. The results confirm that, despite its limitations, μ-XRF can deliver accurate and reproducible data, supporting its use as a rapid and versatile method for *in-situ* compositional analysis of ancient glass.

1. Introduction

This study aims to demonstrate the effectiveness of micro-X-ray fluorescence spectroscopy (μ-XRF) as a reliable, non-invasive technique for the *in-situ* compositional analysis of ancient glass artifacts. Although μ-XRF is accessible and non-destructive, it has limited sensitivity to light elements. To address this, a systematic comparison was conducted with Laser Ablation Inductively Coupled Plasma Mass Spectrometry (LA-ICP-MS), a highly sensitive, laboratory-based technique that requires microsampling of the material for analysis, whereas μ-XRF measures the surface composition without any sampling.

Compositional analysis of ancient glass is key to understanding its manufacturing technology, raw materials used, and their provenance. While major and minor elements are essential for chronological attribution, trace elements, impurities from raw materials, are crucial for identifying material sources or geographical localisation of primary glassmaking furnaces [1,2]. These trace elements also offer valuable insights into archaeological and socio-economic aspects, such as trade routes and inter-societal connections.

Comprehensive characterisation of glass artifacts often requires a combination of analytical techniques [2], with an increasing preference for rapid, portable methods due to the fragility of these items and the challenges associated with sampling, especially when surfaces are heavily altered. In this context, comparative studies [3–6] have shown that selecting the most appropriate analytical approach involves carefully balancing sensitivity, preservation of material, and the desired depth of compositional information [7].

Among portable instruments, μ-XRF represent a widely adopted technique for analysing archaeological glass, valued for its versatility, rapid acquisition, and sensitive multi-elemental analysis with detection limits in the ppm region [8,9]. Its primary advantage in analysing archaeological materials, particularly those prone to surface corrosion,

* Corresponding authors.

https://doi.org/10.1016/j.sab.2025.107449
Received 28 October 2025; Received in revised form 22 December 2025; Accepted 29 December 2025
Available online 6 January 2026

is the ability to examine a microscopic area that has been pre-treated to remove surface deterioration products, ensuring more representative results. Portable μ-XRF spectrometers, typically equipped with polycapillary X-ray lenses operating under atmospheric pressure, have limitations in detecting light elements such as Na, Mg, and Al since X-rays do not reach the detector [10,11]. The limited analytical sensitivity for light elements, which emit low-energy (soft) X-rays, is primarily a consequence of performing measurements in ambient air. Helium purging (flushing) in front of the detector is therefore commonly used to substantially enhance the detected signal, because the characteristic X-rays of light elements would otherwise undergo strong attenuation along the air path (transmission of ~1.3 % to 23.8 % per centimetre for X-rays in the 1–1.5 keV range). In addition, in μ-XRF configurations the transmission efficiency of polycapillary optics drops for soft X-rays because multiple total-reflection steps amplify the effects of reflectivity losses, wall roughness, and geometric distortions, further weakening the already low Rh L-line flux and thus the fluorescence signal from light elements [12]. However, they are highly effective for detecting minor and trace elements, making μ-XRF a valuable tool for preliminary qualitative or semi-quantitative analysis, often complemented by other techniques.

Several studies have indicated that μ-XRF alone is insufficient for comprehensive glass analysis. This limitation has led to the frequent combination of μ-XRF with Scanning Electron Microscopy coupled with Energy Dispersive X-ray Spectroscopy (SEM-EDX), which enables more reliable detection of light elements and provides detailed physical and morphological information [10]. Additionally, μ-XRF is often integrated with LA-ICP-MS [13–16], which enhances elemental coverage, offers high sensitivity, and mitigates the impact of altered surface layers through soft pre-ablation [15].

This study introduces an innovative approach by employing LA-ICP-MS as a reference method to systematically assess the accuracy of μ-XRF in detecting major, minor, and trace elements in archaeological glass. The comparative analysis provides also detailed insights into the analytical range, detection limits, accuracy, and precision of both techniques. In doing so, this research not only highlights the potential of μ-XRF as a rapid and non-invasive method but also establishes it as a reliable tool for *in situ* quantitative analysis. Thus, the key contribution of this study is that having demonstrated μ-XRF's ability to produce data comparable to LA-ICP-MS and proven its capability in preliminary glass classification without compromising analytical quality, this technique can be confidently used for on-site characterisation, reserving LA-ICP-MS for specific cases.

2. Materials and methods

2.1. Materials

To validate the μ-XRF quantitative protocol, this study analysed not only certified reference materials (CRM) but also a set of 36 Roman glass fragments from Aquileia (northeastern Italy), dating from the 1st century BCE to the 4th century CE. The assemblage includes raw glass chunks, production residues, and artefact shards, showcasing a variety of colours, shape, and sizes. Each fragment was sampled to a maximum dimension of 1 cm^3, then embedded in epoxy resin and meticulously polished to ensure a flat, uniform surface suitable for analysis. For efficiency and consistency, three to five fragments were mounted in each resin disk. Sampling and embedding in epoxy resin were necessary for LA-ICP-MS, which requires flat or near-flat surface for accurate analysis, while μ-XRF could technically have been carried out directly on the original artifacts. To ensure consistent measurement conditions and simplify sample transport (given that μ-XRF was performed in Athens, Greece, and LA-ICP-MS in Venice, Italy), the same samples were analysed with both techniques.

2.2. Methods

2.2.1. Micro-X-ray fluorescence spectrometry (μ-XRF)

The μ-XRF analyses were performed using a customised version of the Artax (Bruker AXS) micro-XRF spectrometer at the National Centre for Scientific Research (NCSR) "Demokritos", Athens (Greece). The spectrometer probe consists of an X-ray microfocus Rh-anode tube (anode spot size 50 × 50 μm, max 50 kV, max 1 mA, 30-W maximum power consumption, Be window 0.2-mm thickness) and a polycapillary X-ray lens (IfG) with a focal distance of about 21.2 mm. The X-ray detection system includes an electrothermally cooled 10-mm^2 silicon drift detector (X-Flash, 1000B) with 146 eV FWHM at 10 kcps coupled with a digital signal processor. A colour CCD camera (approximately ×13 magnification) combined with a dimmable white LED and a spot laser beam assures the reproducible positioning of the measuring probe, as well as the visualisation and documentation of the analysed area. Three stepping motors, coupled with the spectrometer head, allow three-dimensional movement for advanced elemental mapping, and precise alignment of the analysis spot at the focal distance of the polycapillary lens.

The acquisition of the spectra was obtained using 50 kV accelerating voltage and 600 μA tube current. The region of interest (ROI) covered is 1 mm^2, consisting of 36 spots spaced 0.2 mm apart, with an acquisition (live) time of 1008 s per ROI, corresponding to 28 s per spot. The μ-XRF measurements are intrinsically robust and, under controlled conditions, are not affected by whether the analysis is performed in the laboratory or *in-situ*. For portable and handheld XRF instruments, analytical performance is independent of the measurement environment, provided that proper conditions are ensured. The hardware design of portable μ-XRF instruments differs substantially from that of laboratory desktop systems, and this distinction motivates the present comparison. The aim of this study is to assess whether a portable μ-XRF spectrometer provides reliable quantitative results for glass materials under controlled sample conditions (embedded, polished specimens).

The sampling depth on silicate glass mainly depends on the energy of the detected X-ray signals, ranging from 1 to 2 μm for light elements to several hundred μm for heavy elements. The μ-XRF spatial resolution is ~75 μm at Cu-Kα (8.04 keV) and ~30 μm at Sn-Kα (25.1 keV). Quantification was conducted using PyMca software, applying the Fundamental Parameter (FP) method and accounting for the relative transmission efficiency of the polycapillary lens, as described by [17]. To ensure the accuracy and stability of μ-XRF measurements, CRM from the Bundesanstalt für Materialforschung und -prüfung (BAM, Federal Institute for Materials Research and Testing) S005—B and the Corning Museum of Glass (CMG) A were analysed at the beginning and end of each session. BAM S005—B was used to assess the daily precision of the instrument for Si, K, Ca, Fe, Cu, Zn, and Sr, while CMG A was employed for Sn, Sb and Pb. Additionally, measurements of BAM S005—B collected throughout the campaign were used to fine-tune the PyMca free parameter "flux", which defines the absolute intensity of the exciting beam. BAM S005—B and CMG A, along with CMG B, were then analysed and compared with their certified values to verify measurement accuracy. This cross-comparison further reinforced data reliability and ensured the consistency of the analytical results. For the correction of Sn and Sb data, CMG A and CMG B were used for Sb, and only CMG B for Sn, as the concentrations of these elements in BAM S005—B are below the limit of quantification (LOQ) (Table SI1 in *Supplementary Information*). The total uncertainty in the reported μ-XRF data for the reference materials arises from two primary independent sources: the statistical uncertainty associated with peak area counting, and the variability in the mean flux parameter over the measurement campaign. Statistical uncertainty, derived from peak area statistics, is typically below 2 %, though it may reach up to 3 %. The second source, reflecting the standard deviation of the mean flux value, is approximately 3 %. Given that these two sources are independent, the combined relative uncertainty was calculated quadratically.

2.2.2. Laser ablation inductively coupled mass spectrometry (LA-ICP-MS)

The LA-ICP-MS instrument used in this research is based in Ca' Foscari University of Venice, Venice (Italy) and consists of an Analyte Excite ArF excimer 193 nm laser (Teledyne CETAC Photon Machines) coupled to an iCAP-RQ quadrupole ICP-MS (Thermo Scientific). The laser ablation device was equipped with a HelEx II two-volume ablation cell mounted on a high-precision xy translating stage. The samples were placed and fixed on a laser ablation holder. A rapid aerosol transfer line (ARIS, Teledyne CETAC Technologies) and helium as carrier gas were used to transport the ablated materials from the surface of the sample to the torch of ICP-MS. The sampling depth on silicate glass can be roughly assumed to be 0.5–1 μm. Assuming a homogeneous composition of the samples, elemental analysis was performed in line scanning mode to determine the bulk elemental oxide composition of the glass samples. Table 1 provides the operational parameters used for the spot drilling procedure. A pre-ablation step was performed to remove superficial dust, using the same ablation parameters, but with a larger spot size and higher repetition rate. Quantification of elements (as their elemental oxides) in the glass samples was performed using a sum normalisation calibration protocol [18]. The method described by van Elteren et al. arbitrarily assumed an internal standard concentration of SiO_2 as 50 wt %. Then the normalisation algorithm adjusts that assumed value based on the sum of all measured oxide concentrations, which equals 100 wt%.

To verify instrument stability and to monitor potential deviations in the analytical setup during each session, CMG A, B, C, D were analysed every 10 samples, while the CRM was measured only at the beginning and end of each session. NIST SRM glass 612 was used also for signal drift correction throughout the ablation. CMG A served for initial calibration, providing a reliable reference for elemental quantification. NIST 612, with certified concentrations for different elements including Rare Earth Elements (REEs), was used to monitor drift. When combined with internal standards like Si, NIST 612 is used for external calibration and it enables correction for variations in ablation efficiency and matrix effects, ensuring accurate trace element quantification throughout the session.

2.2.3. Elaboration of the regression equations

To compare the μ-XRF and LA-ICP-MS data from the archaeological samples and assess the reliability of the μ-XRF measurements relative to LA-ICP-MS, regression equations were established for each element. LA-ICP-MS was selected as the reference technique, and its values were treated as error-free for data processing purposes, despite actual error of about 5 %. Consequently, only μ-XRF measurements were assumed to have experimental uncertainties. Two different approaches were used to model the regression. The first assumed that, for each value of x_i (LA-ICP-MS measured concentration), the corresponding y_i (μ-XRF measured concentration) is distributed with mean $a + bx_i$ (where a is the intercept and b is the slope), with the same variance for all y_i data. The second approach considers different variance for each y_i, arising from uncertainties related in both calibration and the measured quantities, as discussed in *section 2.2.1*. The expected values were $a_{exp} = 0$, and $b_{exp} = 1$.

The second approach, accounting for varying y_i variances, generally improved the data fit outputs (a and b parameters). However, systematic underestimation remained in some cases: possible reasons are the assumptions of error-free x data, uniform 3 % instrumental error across all y elements, the experimental procedures such as the different points of analysis on the glass samples, and the differing sampling depth of the two techniques in nonhomogeneous materials.

Table 1
LA-ICP-MS operational parameters used for glass analysis.

Laser Ablation		*ICP-MS*	
Laser type	ArF excimer 193 nm	RF power	1550 W
He gas flow cell	0.25 L min^{-1}	Cooling gas flow	14 L min^{-1}
He gas flow cup	0.25 L min^{-1}	Auxiliary gas flow	0.8 L min^{-1}
Transfer line	ARIS	Ar makeup gas flow	0.8 L min^{-1}
Spot size	135 μm (pre-ablation), 40 μm (ablation)	Monitored isotope masses	^{3}Li, ^{4}Be, ^{7}B, ^{11}Na, ^{12}Mg, ^{13}Al, ^{14}Si, ^{15}P, ^{19}K, ^{20}Ca, ^{21}Sc, ^{22}Ti, ^{23}V, ^{24}Cr, ^{25}Mn, ^{26}Fe, ^{27}Co, ^{28}Ni, ^{29}Cu, ^{30}Zn, ^{31}Ga, ^{33}As, ^{34}Se, ^{37}Rb, ^{38}Sr, ^{39}Y, ^{40}Zr, ^{41}Nb, ^{42}Mo, ^{47}Ag, ^{48}Cd, ^{49}In, ^{50}Sn, ^{51}Sb, ^{56}Ba, ^{57}La, ^{58}Ce, ^{59}Pr, ^{60}Nd, ^{62}Sm, ^{63}Eu, ^{64}Gd, ^{65}Tb, ^{66}Dy, ^{67}Ho, ^{68}Er, ^{69}Tm, ^{70}Yb, ^{71}Lu, ^{79}Au, ^{82}Pb, ^{83}Bi, ^{90}Th, ^{92}U
Fluence	6 J/cm^2 (pre-ablation), 4 J/cm^2 (ablation)		
Repetition rate	30 Hz (pre-ablation), 20 Hz (ablation)		
Scanning mode	Continuous line		
Ablation mode	Fixed dosage 10		

3. Results and discussion

3.1. Daily precision of μ-XRF

Multiple measurements were performed using BAM S005—B and Corning A reference materials to evaluate the daily precision of μ-XRF. BAM S005 was analysed at both the beginning and the end of each session, and was used for Si, K, Ca, Fe, Cu, Zn, and Sr, while CMG-A was measured only at the beginning of each session and served as reference for Sn, Sb and Pb. To assess measurement variability, the mean, standard deviation and 2σ error were calculated and plotted together with the daily measurements, as shown in Fig. 1 for some major and minor elements (Fe, Cu, Zn, and Sr plots are presented in Figure SI1 in *Supplementary Information*). Since BAM S005—B was measured more frequently within each session, it appears more often in the dataset than CMG-A. Before calculating concentrations, the raw peak area data were investigated. This was necessary to assess the instrument's performance accurately: peak area stability reflects the fundamental precision of the μ-XRF system, while consistent concentration values demonstrate the robustness of the quantification procedure. The trend comparison showed variations within one standard deviation, confirming the stability of the instrument's operating conditions as well as the reproducibility of the sample repositioning on the reference sample.

The parallel trends observed in the two datasets indicate that the stability of the raw spectral measurements translate directly into consistent concentration values. This reinforces the reliability of the μ-XRF method under normal operating conditions, while also showing that variations in peak area directly affect the accuracy of the quantification process. Overall, μ-XRF delivered reliable and repeatable elemental analyses, with most variations remaining within acceptable limits.

3.2. Analysis of Corning reference glasses

The quantification procedures for both μ-XRF and LA-ICP-MS analyses were validated by comparing the results obtained for CMG A and B for elements above the limit of detection (LOD) (Tables 2 and 3). Certified reference values and concentrations measured by both techniques are presented in Tables 2 and 3, while μ-XRF results for BAM S005—B compared against its reference values, are given in Table 4. Specifically, Tables 2 and 3 summarise the measured concentrations, relative standard deviations (RSD), and bias values for Corning A and B glasses, providing a quantitative assessment of the accuracy and precision of both μ-XRF and LA-ICP-MS methods.

Overall, the comparison across major, minor, and trace elements in the reference materials shows good consistency for most components. As reported in Tables 2 and 3, μ-XRF measurements exhibit variable biases, both positive and negative, with relative standard deviations generally within acceptable ranges, confirming reliable analytical performance.

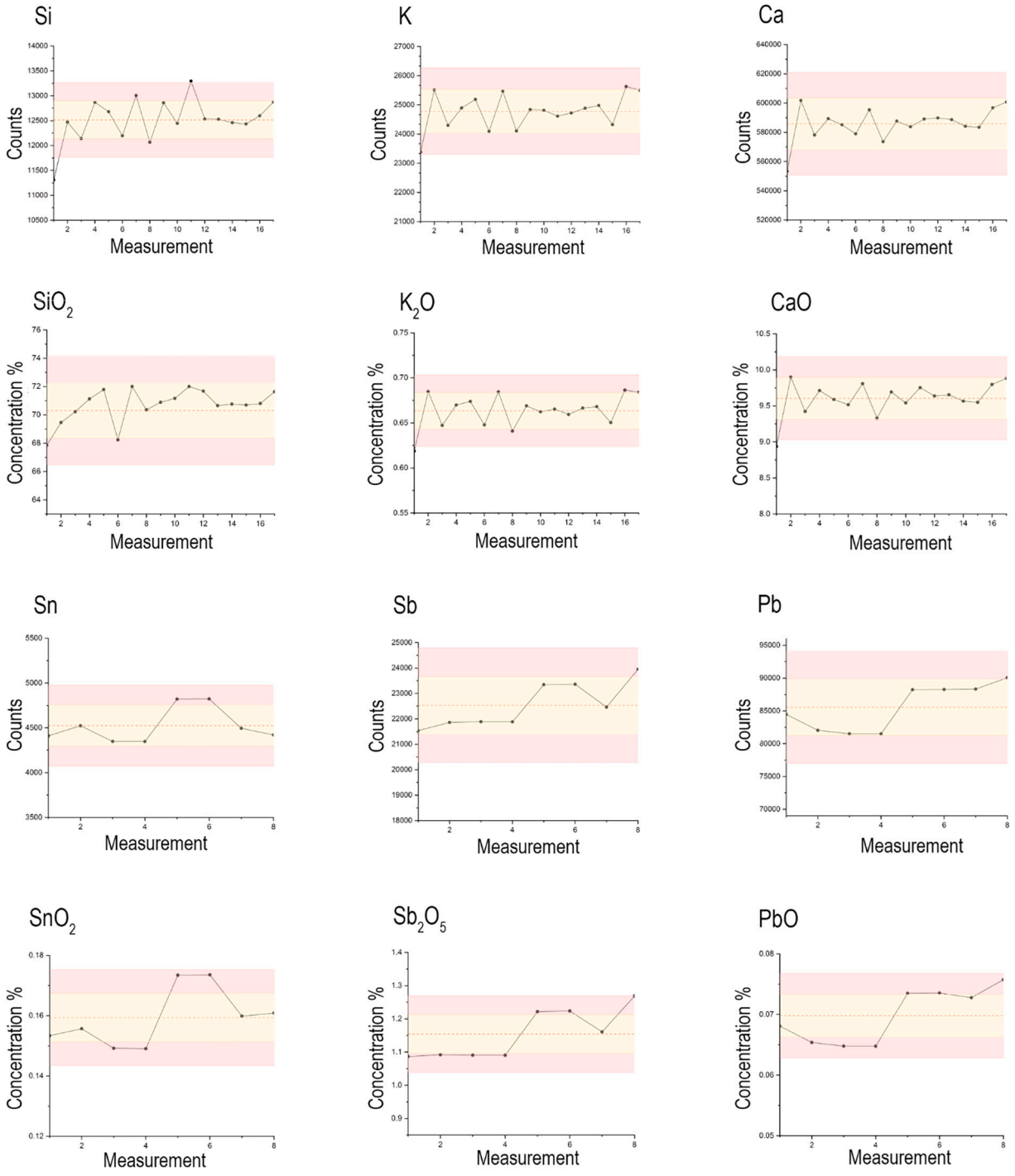

Fig. 1. Daily precision of μ-XRF measurements for elements (fit peak area) and their corresponding oxides (concentration). The black line with markers represents the daily values, the red dashed line indicates the mean, yellow area shows 1σ as 3 % for Si/SiO_2, K/K_2O an Ca/CaO and 5 % for the rest, and the pink area represents the 2σ error range. (For interpretation of the references to colour in this figure legend, the reader is referred to the web version of this article.)

However, it should be noted that for a small number of elements (Sr, Zr, Ba, and Pb) in Corning A and B glasses, the observed percentage bias, positive for Zr and Sr and negative for Ba and Pb, is of very similar magnitude for both techniques. This may indicate either greater inhomogeneity for these elements within the glasses or a systematic offset in the respective nominal (certified) values. LA-ICP-MS shows excellent agreement with the certified values, with minimal deviations for most elements, albeit with a few exceptions. Both techniques demonstrate high precision, as indicated by low RSDs (~1.6 %), and good accuracy, as reflected by the reported bias values.

The bias trends are further illustrated in Fig. 2, which reports the ratios between μ-XRF and LA-ICP-MS results and the certified values for Corning A (Fig. 2a) and Corning B (Fig. 2b) glasses. To visualise these results, the ratio between the certified value and the values obtained from μ-XRF and LA-ICP-MS were calculated and reported in Fig. 2a-b (Radar plot of BAM S005—B in Figure SI3 in *Supplementary Information*). Ratios close to 1 indicates strong agreement with the reference value, and while most elements fall within this range, confirming consistent measurement performance, certain elements exhibit significant deviations.

Table 2
Certified values of Corning A and concentrations measured by μ-XRF and LA-ICP-MS, expressed in wt%. The relative error (%) reflects the total uncertainty, accounting for both the 3 % calibration uncertainty and the variability observed in replicated measurements performed on different days. The μ-XRF relative error is 3 % for all oxides, except for Rb_2O, ZrO_2, and SnO_2, for which it is 4 %. The relative standard deviation (RSD, %) reflects measurement repeatability. Relative bias (%) is reported as the difference between the measured and certified values, expressed as a percentage of the certified value. LOQ is expressed as 3*LOD.

	Corning A					
	Certified values	μ-XRF	Relative standard deviation (RSD) %	μ-XRF relative bias %	LA-ICP-MS	LA-ICP-MS relative bias %
SiO_2	66.56	64.47	2.7	−3.1	66.78	0.3
K_2O	2.87	2.47	4.6	−13.9	2.98	3.8
CaO	5.03	4.3	4.9	−14.5	5.19	3.2
TiO_2	0.79	0.70	5.0	−11.4	0.79	0.0
MnO	1.00	0.92	6.0	−8.0	1.03	3.0
FeO	1.09	0.88	5.3	−19.3	1.10	0.9
CoO	0.13	0.16	6.0	23.1	0.18	38.5
NiO	0.02	0.02	6.8	0.0	0.03	50.0
CuO	1.17	1.12	5.7	−4.3	1.15	−1.7
ZnO	0.044	0.046	4.9	4.5	0.05	13.6
Rb_2O	0.01	0.01	6.3	0.0	0.01	0.0
SrO	0.10	0.11	6.3	10.0	0.10	0.0
ZrO_2	0.005	0.011	9.7	120.0	0.01	100.0
SnO_2	0.19	0.16	6.1	−15.8	0.19	0.0
Sb_2O_5	1.75	1.46	6.5	−16.6	1.77	1.1
BaO	0.50	0.36	5.5	−28.0	0.44	−12.0
PbO	0.12	0.07	6.5	−41.7	0.06	−50.0

Table 3
Certified values of Corning B and concentrations measured by μ-XRF and LA-ICP-MS, expressed in wt%. The relative error (%) reflects the total uncertainty, accounting for both the 3 % calibration uncertainty and the variability observed in replicated measurements performed on different days. The μ-XRF relative error is 3 % for all oxides, except TiO_2, CoO and BaO which is 4 %. The relative standard deviation (RSD, %) reflects measurement repeatability. Relative bias (%) is reported as the difference between the measured and certified values, expressed as a percentage of the certified value. LOQ is expressed as 3*LOD.

	Corning B					
	Certified values	μ-XRF	Relative standard deviation (RSD) %	μ-XRF relative bias %	LA-ICP-MS	LA-ICP-MS relative bias %
SiO_2	61.55	63	1.2	2.4	62.51	1.6
K_2O	1.00	0.99	0.7	−1.0	1.01	1.0
CaO	8.56	8.1	0.9	−5.4	8.57	0.1
TiO_2	0.09	0.10	1.3	11.1	0.11	22.2
MnO	0.25	0.24	0.5	−4.0	0.22	−12.0
FeO	0.34	0.31	0.7	−8.8	0.36	5.9
CoO	0.046	0.04	2.0	−13.0	0.04	−13.0
NiO	0.10	0.09	1	−10.0	0.10	0.0
CuO	2.66	2.84	0.7	6.8	2.70	1.5
ZnO	0.19	0.20	0.5	5.3	0.19	0.0
SrO	0.019	0.02	1.0	5.3	0.02	5.3
ZrO_2	0.03	0.03	6.6	0.0	0.03	0.0
SnO_2	0.04	<LOD	–	–	0.03	−25.0
Sb_2O_5	0.46	0.46	4.3	0.0	0.43	−6.5
BaO	0.12	0.08	6.6	−33.3	0.07	−41.7
PbO	0.61	0.47	0.9	−23.0	0.40	−34.4

For both reference materials, μ-XRF ratios group around unity for most major and minor oxides, confirming overall good agreement with certified compositions. In Corning A (Fig. 2a), μ-XRF shows a systematic tendency toward negative bias for several oxides while pronounced positive deviations are observed for selected trace elements such as ZrO_2, consistent with the large relative biases reported in Table 2.

Table 4
Certified values of BAM S005—B and concentrations measured by μ-XRF, expressed in wt% and ppm. The relative error (%) reflects the total uncertainty, accounting for both the 3 % calibration uncertainty and the variability observed in replicated measurements performed on different days. The reported uncertainty (ppm) is provided by the manufacturer of the CRM, while the μ-XRF relative error is is 3 % for all oxides, except V_2O_5, MnO, NiO, As_2O_3 and PbO which is 4 % and for TiO_2 and CoO is 5 %. The relative standard deviation (RSD, %) reflects measurement repeatability. Relative bias (%) is reported as the difference between the measured and certified values, expressed as a percentage of the certified value. LOQ is expressed as 3*LOD. *Not certified, informative values.

	BAM S005-B					
	Unit	Certified values	Uncertainty (ppm)	μ-XRF	Relative standard deviation (RSD) %	μ-XRF relative bias %
SiO_2*	%	71	–	70	2.7	−1.4
K_2O*	%	0.7	–	0.66	3.9	−5.7
CaO*	%	10.5	–	9.5	4.0	−9.5
TiO_2	ppm	163	9	163	6.4	0.0
V_2O_5	ppm	349	22	345	4.6	−1.1
MnO	ppm	124	5	120	6.0	−3.2
Fe_2O_3	ppm	422	11	380	4.7	−10.0
CoO	ppm	49.4	2.4	52	6.1	5.3
NiO	ppm	59.0	2	60	7.9	1.7
CuO	ppm	112	5	120	5.7	7.1
ZnO	ppm	203	10	234	4.7	15.3
As_2O_3	ppm	132	8	165	5.3	25.0
SrO	ppm	151	7	185	6.6	22.5
ZrO_2	ppm	842	125	1002	7.2	19.0
MoO_3	ppm	343	12	408	8.3	19.0
PbO	ppm	202	8	200	9.6	−1.0

However, the overlap between the Zr-Kα and Sr-Kβ lines could introduce significant error, given that the Sr concentration is over 11 times higher than that of Zr. PbO ratios obtained by both μ-XRF and LA-ICP-MS show underestimation. For μ-XRF, this may stem from the low concentration of Pb in the reference material. For LA-ICP-MS, the underestimation of PbO concentration is likely due to fractionation effects during laser ablation and transport processes, where the size distribution of particles generated during laser ablation affects transport and ionisation efficiency in the ICP, potentially leading to elemental fractionation [19,20]. These processes may result in a systematic underestimation of PbO in LA-ICP-MS analyses, particularly when present in low concentrations. These effects are due to the low concentration levels and proximity to the detection limits, where small absolute differences result in amplified relative deviations. In contrast, for Corning B (Fig. 2b), the ratios from μ-XRF and LA-ICP-MS are more consistent, with only a few oxides deviating from the certified values. Deviations remain moderate for most oxides, with slightly larger biases observed for BaO, PbO, and selected trace components. In contrast, LA-ICP-MS ratios remain close to unity for nearly all elements in both reference materials, reflecting its higher sensitivity and lower susceptibility to matrix and detection-limit effects.

Overall, the radar plots corroborate the tabulated bias values and further support the robustness and quantitative reliability of μ-XRF under controlled conditions, particularly for major and minor glass constituents.

3.3. Comparison between μ-XRF and LA-ICP-MS data of archaeological glass

The analysis of the archaeological samples followed the same approach, considering only oxides that can be detected by both techniques, as μ-XRF cannot detect Na, Mg and Al compared to LA-ICP-MS. However, a comparison between the μ-XRF residual matrix and the LA-ICP-MS Na_2O + MgO + Al_2O_3 wt% sum is provided in Table SI2 in

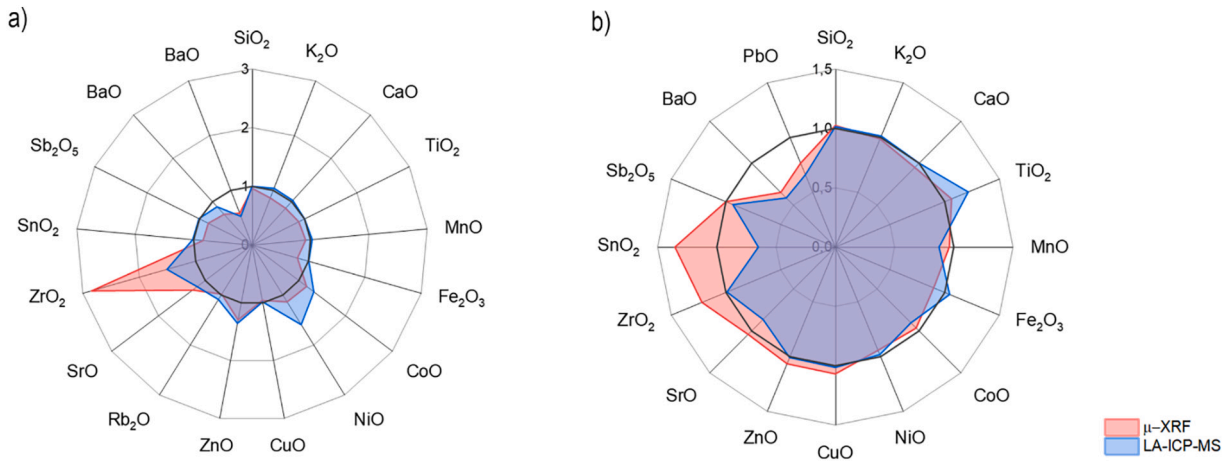

Fig. 2. Radar plot of major, minor and trace elements of (a) Corning A and (b) Corning B expressed as ratio between the value obtained using μ-XRF and LA-ICP-MS and the respective certified value of the reference material.

Supplementary Information, demonstrating the close agreement between the μ-XRF residual-matrix and the LA-ICP-MS oxide sum. Table 5 reports the chemical composition of the archaeological glass as determined by μ-XRF and LA-ICP-MS. For Ba, although LA-ICP-MS detected concentrations above ~40 ppm, μ-XRF measurements were excluded because strong spectral interferences from Ti significantly increase the effective detection limit, preventing reliable quantification. However, overall, the two datasets show good correlation, with the exceptions of SnO_2 and Sb_2O_5, which are discussed separately in *section 3.4*.

Results obtained from the archaeological glass analysis by both techniques were compared in scatterplots (Fig. 3 a-l), which include a linear regression equation and the coefficient of determination (R) (Table 6). As discussed in *section 2.2.3* regarding the treatment of analytical uncertainties, the variable-error approach, which accounts for element-specific variances in the μ-XRF measurements, generally improved the regression parameters. However, this method may over- or under-estimate the true uncertainty for different elements, and residual systematic underestimation remained in several cases. For this reason, the simpler constant-error model was ultimately preferred for consistency and reliability, using the equations reported in Figure SI2 in *Supplementary Information*. Estimating μ-XRF uncertainty is inherently challenging, as it depends both on the limited variability at different points of the same sample and, more importantly, on variability among different glass samples. The combination of uncertain μ-XRF errors and the assumption of zero error for LA-ICP-MS can distort regression outcomes, likely contributing to discrepancies observed with the variable-error model. Additionally, for some elements, the concentration ranges were narrow and did not cover the full compositional scale uniformly. For example, SiO_2 ranged from ~48–77 wt%, while other elements started near zero. This partial coverage limits the generalizability of slope and intercept parameters across the entire range. In this comparison, a slope value close to 1 indicates good agreement between techniques, while R values approaching 1 reflect strong linearity and reproducibility.

All the major oxides in the glass composition exhibit R values above 0.8. Similarly, for the calculated intercept values, which should be compatible with 0 within the experimental uncertainties, most elements show acceptable values, except for ZrO_2 and PbO. For the trace elements SrO and ZrO_2, the plots show more variability, with data largely scattered around the best fit line. For SrO, R value suggests a limited goodness of the initial working hypothesis. ZrO_2 shows a strong R value, but a non-zero intercept value suggests a moderate systematic overestimation by μ-XRF compared to LA-ICP-MS data. These results indicate that, while μ-XRF and LA-ICP-MS are broadly comparable for most oxides, some elements require caution in direct cross-technique data interpretation.

Considering the scatterplot and linear regression of the oxides of the archaeological samples obtained by both techniques, along with the results presented in previous sections regarding the daily precision of μ-XRF and its validation using CRM, the robustness and reliability of μ-XRF was demonstrated. Based on this statement, μ-XRF was confidently applied to investigate Roman archaeological glass samples, allowing to make considerations regarding the raw materials employed, such as sand, fluxes, and colourants, as well as their provenance, as discussed in the following text.

μ-XRF data indicate that the archaeological samples can be attributed to a typical Roman glass production. CaO concentration ranges from 6 to 8 %, aligning with Low Magnesium Glass (LMG) classification [21]. As for the flux source, most of the samples presents K_2O concentration below 2 %, while only few samples display a higher concentration (>4–5 %). This would suggest the possible use of two different fluxes, potentially natron and plant ash. When natron is used, K_2O remains below 1.5 %, whereas plant ash results in concentrations above 3 % [21]. This information, together with the CaO concentration may suggest that the few samples with elevated K_2O levels may correspond to High Magnesium Glass (HMG), though MgO data are not available. Since Na_2O and MgO cannot be detected by μ-XRF, the alkali source cannot be conclusively determined; however, speculation and hypothesis can be accurately made based on the other major elements.

Regarding the evaluation of samples' colour, μ-XRF data obtained for the minor elements that characterise the glass composition indicated the oxides responsible for glass colouration. For example, Cu contributes to the blue colouration in some blue glass samples, while a combination of Cu and Co produces a deep blue [22], and purple glass shows high Fe and Mn concentrations [23]. Emerald green, typically produced in the early 1st century CE for luxury and decorative items, results from multiple colouring and opacifying agents like Cu, Fe, Pb, Sn, and Sb, and the addition of plant ash to the natron-based glass batch [24]. High Pb levels are present in yellow translucent and opaque glass [25]. The identification of different opacifiers, such as Sb_2O_5 and SnO_2, is particularly significant, highlighting the historical transition from antimony- to tin-based opacifiers [26].

Furthermore, trace elements also provide insights into raw material selection and their provenience [1], facilitating a more accurate determination of sand composition. In particular, the concentration of Sr, which is associated with the presence of aragonite from seashell, is significant for understanding the provenience of the silica source used. Correlations between CaO and Sr data, as well as Sr and Zr, suggest that mainly a single sand source was used in the production of these glass fragments. High concentration of Sr (300–600 ppm) with low

Table 5
Comparison of the chemical composition of archaeological glass determined by μ-XRF and LA-ICP-MS. For SnO_2 and Sb_2O_5, both the uncorrected (values in brackets) and corrected concentrations are reported.

			SiO_2	K_2O	CaO	TiO_2	Cr_2O_3	MnO	Fe_2O_3	CoO	CuO	ZnO	As_2O_3	Rb_2O	SrO	ZrO_2	SnO_2	Sb_2O_5	BaO	PbO
	Unit		%	%	%	%	ppm	%	%	ppm	%	ppm	ppm	ppm	ppm	ppm	%	%	ppm	%
	μ-XRF relative error (%)		3	3	3	3	4	3	3	3	3	4	3	4	3	3	4	4	–	3
AG1	Emerald green	μ-XRF	64	1.12	6.1	0.13	–	0.67	0.97	–	1.90	250	–	–	680	165	(0.15) 0.20	(0.05) 0.12	–	0.03
		LA-ICP-MS	65.8	1.02	6.6	0.14	–	0.67	1.31	–	1.77	156	–	–	567	79	0.18	0.08	252	0.02
AG2	Emerald green	μ-XRF	64	1.24	5.7	0.15	–	0.57	1.02	–	2.27	180	–	–	620	124	(0.12) 0.16	–	–	0.04
		LA-ICP-MS	66.5	1.19	6.6	0.17	–	0.55	1.46	–	2.31	86	–	–	649	96	0.11	0.05	252	0.04
AG3	Emerald green	μ-XRF	61	1.33	5.8	0.14	–	0.67	1.25	–	2.22	200	–	–	530	135	(0.18) 0.25	–	–	0.03
		LA-ICP-MS	63.7	1.40	7.1	0.17	–	0.74	1.47	–	2.43	125	–	–	560	105	0.22	0.01	256	0.03
AG4	Emerald green	μ-XRF	65	1.61	6.4	0.18	–	0.81	1.44	–	2.30	280	–	–	570	144	(0.21) 0.28	(0.08) 0.17	–	0.09
		LA-ICP-MS	66.8	1.50	6.8	0.17	–	0.80	1.49	–	1.71	186	–	–	514	115	0.19	0.08	324	0.08
AG5	Emerald green	μ-XRF	64	1.31	7.5	0.25	–	0.89	1.33	–	2.32	–	–	–	570	201	(0.23) 0.31	(0.11) 0.21	–	0.17
		LA-ICP-MS	63.8	1.25	8.3	0.25	–	0.98	1.55	–	1.89	–	–	–	571	183	0.25	0.11	619	0.17
AG6	Emerald green	μ-XRF	65	0.59	5.6	0.09	–	0.30	0.60	–	2.40	–	–	–	330	59	(0.09) 0.12	(0.31) 0.55	–	1.25
		LA-ICP-MS	65.7	0.64	6.9	0.11	–	0.27	0.75	–	2.64	–	–	–	457	78	0.13	0.56	216	2.02

			SiO_2	K_2O	CaO	TiO_2	Cr_2O_3	MnO	Fe_2O_3	CoO	CuO	ZnO	As_2O_3	Rb_2O	SrO	ZrO_2	SnO_2	Sb_2O_5	BaO	PbO
	Unit		%	%	%	%	ppm	%	%	ppm	%	ppm	ppm	ppm	ppm	ppm	%	%	ppm	%
	μ-XRF relative error (%)		3	3	3	3	4	3	3	3	3	4	3	4	3	3	4	4	–	3
AG7	Red	μ-XRF	64	0.49	5.6	0.10	–	0.84	3.50	–	0.47	–	–	–	410	134	(0.17) 0.24	(0.12) 0.23	–	1.46
		LA-ICP-MS	64.4	0.90	6.7	0.10	–	0.90	4.01	–	0.44	113	173	–	457	77	0.29	0.22	358	1.47
AG8	Blue	μ-XRF	64	0.57	5.8	0.07	–	0.27	0.64	–	2.54	150	–	–	360	120	(0.12) 0.16	(1.70) 2.90	–	0.08
		LA-ICP-MS	66.2	0.63	6.6	0.11	–	0.22	0.85	–	3.08	64	78	–	415	86	0.17	2.63	181	0.09
AG9	Colourless	μ-XRF	72	0.64	7.6	0.08	–	1.35	0.36	–	–	–	–	–	720	105	–	–	–	–
		LA-ICP-MS	71.7	0.36	7.3	0.06	–	1.30	0.38	–	–	–	–	–	488	50	–	–	482	–
AG10	Amber	μ-XRF	70	0.48	7.7	0.05	–	0.02	0.27	–	–	–	–	–	560	141	–	–	–	–
		LA-ICP-MS	70.1	0.33	8.8	0.06	–	0.02	0.38	–	–	–	–	–	488	90	–	–	209	–
AG11	Amber	μ-XRF	72	0.59	11.2	0.03	–	0.01	0.07	–	–	–	–	–	–	–	–	–	–	–
		LA-ICP-MS	72.3	0.48	10.9	0.03	–	0.01	0.12	–	–	–	–	–	–	–	–	–	120	–
AG12	Brown	μ-XRF	62	0.61	4.7	0.32	45	0.13	1.30	–	–	–	–	–	520	294	–	–	–	–
		LA-ICP-MS	65.5	0.42	5.1	0.30	57	0.13	1.61	–	–	–	–	–	365	187	–	–	189	–

			SiO_2	K_2O	CaO	TiO_2	Cr_2O_3	MnO	Fe_2O_3	CoO	CuO	ZnO	As_2O_3	Rb_2O	SrO	ZrO_2	SnO_2	Sb_2O_5	BaO	PbO
	Unit		%	%	%	%	ppm	%	%	ppm	%	ppm	ppm	ppm	ppm	ppm	%	%	ppm	%
	μ-XRF relative error (%)		3	3	3	3	4	3	3	3	3	4	3	4	3	3	4	4	–	3
AG13	Brown	μ-XRF	68	0.83	3.8	0.17	–	0.31	0.91	–	–	–	–	–	390	241	–	–	–	–
		LA-ICP-MS	69.3	0.56	4.0	0.15	–	0.28	1.10	–	–	–	–	–	262	126	–	–	193	–

(*continued on next page*)

Table 5 (*continued*)

			SiO_2	K_2O	CaO	TiO_2	Cr_2O_3	MnO	Fe_2O_3	CoO	CuO	ZnO	As_2O_3	Rb_2O	SrO	ZrO_2	SnO_2	Sb_2O_5	BaO	PbO
Unit			%	%	%	%	ppm	%	%	ppm	%	ppm	ppm	ppm	ppm	ppm	%	%	ppm	%
AG14	Yellow	μ-XRF	69	0.50	6.8	0.06	–	0.01	0.24	–	–	–	–	–	440	–	–	–	–	–
		LA-ICP-MS	71.7	0.31	7.4	0.05	–	0.01	0.30	–	–	–	–	–	374	–	–	–	203	–
AG15	Brown	μ-XRF	61	1.23	5.5	0.23	–	0.40	1.27	–	0.06	–	–	–	550	243	–	–	–	0.04
		LA-ICP-MS	65.6	1.17	6.4	0.23	–	0.40	1.55	–	0.02	–	–	–	456	158	0.01	0.02	237	0.02
AG16	Colourless	μ-XRF	72	1.13	7.0	0.15	–	0.46	0.71	–	0.07	80	–	–	520	171	–	–	–	0.02
		LA-ICP-MS	71.1	1.03	7.5	0.15	–	0.41	0.83	–	0.05	56	–	48	456	109	0.01	0.08	274	0.02
AG17	Colourless	μ-XRF	69	0.48	6.7	0.06	–	0.16	0.35	–	0.01	–	–	–	520	–	–	–	–	0.02
		LA-ICP-MS	72.6	0.36	8.0	0.06	–	0.17	0.39	–	0.01	–	–	–	450	–	–	0.02	282	0.01
AG18	Colourless	μ-XRF	63	7.69	1.5	0.47	–	0.12	2.32	–	–	136	–	300	450	843	–	–	–	–
		LA-ICP-MS	64.3	7.03	1.9	0.44	–	0.10	2.42	–	–	113	–	234	343	629	–	–	636	–

			SiO_2	K_2O	CaO	TiO_2	Cr_2O_3	MnO	Fe_2O_3	CoO	CuO	ZnO	As_2O_3	Rb_2O	SrO	ZrO_2	SnO_2	Sb_2O_5	BaO	PbO
Unit			%	%	%	%	ppm	%	%	ppm	%	ppm	ppm	ppm	ppm	ppm	%	%	ppm	%
μ-XRF relative error (%)			3	3	3	3	4	3	3	3	3	4	3	4	3	3	4	4	–	3
AG19	Brown	μ-XRF	70	0.74	7.2	0.08	–	0.37	0.44	–	0.07	–	–	–	540	162	–	–	–	0.02
		LA-ICP-MS	70.7	0.58	8.2	0.07	–	0.35	0.45	–	0.11	–	–	–	506	57	–	0.03	240	0.01
AG20	Colourless	μ-XRF	72	0.58	7.3	0.06	–	0.40	0.38	–	–	–	–	–	610	–	–	–	–	–
		LA-ICP-MS	72.3	0.33	7.6	0.05	–	0.26	0.39	–	–	–	–	–	426	–	–	–	206	–
AG21	Blue	μ-XRF	77	6.04	6.4	0.02	–	0.01	0.05	90	2.64	141	–	92	–	–	–	–	–	0.03
		LA-ICP-MS	75.2	5.27	6.3	0.02	–	0.01	0.06	103	2.31	156	129	84	–	–	–	–	–	0.01
AG22	Blue	μ-XRF	67	0.62	7.4	0.06	–	0.75	0.73	610	0.1	–	–	–	630	123	–	–	–	0.01
		LA-ICP-MS	68.4	0.45	8.1	0.06	–	0.74	0.86	425	0.09	–	–	–	515	54	–	0.02	267	0.01
AG23	Blue	μ-XRF	67	0.45	7.2	0.04	–	0.40	0.67	560	0.14	63	145	–	490	133	–	(0.93) 1.60	–	–
		LA-ICP-MS	69.1	0.33	8.1	0.06	–	0.45	0.92	489	0.16	53	140	–	472	52	–	2.28	231	0.01
AG24	Colourless	μ-XRF	67	0.61	6.1	0.08	–	0.45	0.41	–	0.1	–	–	–	510	126	–	(0.18) 0.33	–	0.05
		LA-ICP-MS	71.5	0.49	6.6	0.08	–	0.43	0.50	–	0.1	–	–	–	410	71	–	0.22	189	0.04

			SiO_2	**K_2O**	**CaO**	**TiO_2**	**Cr_2O_3**	**MnO**	**Fe_2O_3**	**CoO**	**CuO**	**ZnO**	**As_2O_3**	**Rb_2O**	**SrO**	**ZrO_2**	**SnO_2**	**Sb_2O_5**	**BaO**	**PbO**
Unit			%	%	%	%	ppm	%	%	ppm	%	ppm	ppm	ppm	ppm	ppm	%	%	ppm	%
μ-XRF relative error (%)			3	3	3	3	4	3	3	3	3	4	3	4	3	3	4	4	–	3
AG25	Blue	μ-XRF	77	7.23	6.7	0.03	54	0.10	0.10	–	1.99	154	320	122	–	–	–	–	–	–
		LA-ICP-MS	76.2	6.93	6.9	0.02	65	0.09	0.12	–	1.78	58	331	109	–	–	–	–	136	0.01
AG26	Amber	μ-XRF	69	0.46	7.0	0.06	–	0.03	0.27	–	–	–	–	–	530	119	–	–	–	0.01
		LA-ICP-MS	69.7	0.30	7.5	0.05	–	0.02	0.31	–	–	–	–	–	403	54	–	–	173	0.01
AG27	Purple	μ-XRF	67	0.82	6.8	0.09	–	2.12	0.80	–	0.31	90	–	–	760	125	–	(0.24) 0.43	–	0.39
		LA-ICP-MS	65.6	0.53	6.9	0.09	–	2.26	0.90	–	0.25	68	59	–	615	72	0.03	0.30	307	0.33
AG28	Blue	μ-XRF	70	1.21	5.2	0.12	–	0.56	0.54	–	0.02	–	–	–	510	150	–	(0.11) 0.21	–	0.02
		LA-ICP-MS	70.6	1.08	5.9	0.11	–	0.56	0.66	–	0.01	–	–	–	380	100	0.51	0.14	274	0.01
AG29	Blue	μ-XRF	69	1.25	7.1	0.07	–	0.36	0.44	–	0.27	–	–	–	570	95	–	–	–	0.03
		LA-ICP-MS	70.6	0.92	7.4	0.07	–	0.37	0.56	–	0.19	–	–	–	412	57	0.02	0.03	263	0.02
AG30	Grey	μ-XRF	69	1.05	7.5	0.07	–	0.37	0.41	–	0.14	–	–	–	580	117	–	–	–	0.02

(*continued on next page*)

Table 5 (*continued*)

		SiO_2	K_2O	CaO	TiO_2	Cr_2O_3	MnO	Fe_2O_3	CoO	CuO	ZnO	As_2O_3	Rb_2O	SrO	ZrO_2	SnO_2	Sb_2O_5	BaO	PbO
	Unit	%	%	%	%	ppm	%	%	ppm	%	ppm	ppm	ppm	ppm	ppm	%	%	ppm	%
	LA-ICP-MS	71.1	0.75	7.4	0.05	–	0.33	0.48	–	0.10	–	–	–	414	51	–	0.01	248	0.01

			SiO_2	K_2O	CaO	TiO_2	Cr_2O_3	MnO	Fe_2O_3	CoO	CuO	ZnO	As_2O_3	Rb_2O	SrO	ZrO_2	SnO_2	Sb_2O_5	BaO	PbO
	Unit		%	%	%	%	ppm	%	%	ppm	%	ppm	ppm	ppm	ppm	ppm	%	%	ppm	%
μ-XRF relative error (%)			3	3	3	3	4	3	3	3	3	4	3	4	3	3	4	4	–	3
AG31	Amber	μ-XRF	71	0.95	6.2	0.05	–	0.14	0.18	–	–	–	–	–	100	228	–	–	–	–
		LA-ICP-MS	72.9	1.02	6.5	0.05	–	0.13	0.20	–	–	–	–	–	68	113	–	–	427	–
AG32	Grey	μ-XRF	69	0.76	7.3	0.05	–	0.77	0.79	400	0.06	62	–	–	520	–	–	–	–	–
		LA-ICP-MS	68.4	0.91	8.5	0.06	–	0.81	0.81	457	0.07	58	–	–	531	–	–	0.21	265	–
AG33	Purple	μ-XRF	66	0.69	6.4	0.05	–	1.17	0.29	–	–	–	571	–	580	–	–	–	–	–
		LA-ICP-MS	70.1	0.82	8.0	0.05	–	1.33	0.37	–	–	–	593	–	643	–	–	–	262	–
AG34	Colourless	μ-XRF	67	2.13	10.4	0.07	–	0.27	0.64	–	0.01	350	–	–	860	–	–	–	–	0.01
		LA-ICP-MS	66.5	2.29	12.4	0.07	–	0.21	0.73	–	0.01	307	–	–	723	–	–	–	245	0.01
AG35	Colourless	μ-XRF	76	0.40	6.7	0.04	–	0.18	0.04	–	–	–	1455	–	–	198	–	–	–	0.33
		LA-ICP-MS	74.7	0.31	7.4	0.04	–	0.13	0.03	–	–	–	1196	–	–	149	–	–	–	0.30
AG36	Purple	μ-XRF	48	3.62	22.9	0.68	161	0.36	4.06	–	0.22	–	–	96	410	–	–	–	–	–
		LA-ICP-MS	51.8	3.68	22.9	0.64	186	0.30	5.34	–	0.17	–	–	60	330	–	0.04	–	–	–

concentrations of Zr (<100 ppm) suggest the use of coastal sand (Egypt), which is different from inland (Levantine) silica sources that generally exhibit higher zircon content [28].The correlation trends of TiO_2 data with both Fe_2O_3 and Zr provide additional information about the type of sand used, reflecting the presence of iron–titanium minerals (ilmenite) and zircons [28–30]. These minerals, commonly found in sand deposits, serve as indicators of sand composition. Correlation between titanium and zirconium helps characterise the mineralogical mark and the composition of the sand used in the production of glass. These findings suggest the use of sand rich in auxiliary minerals such as zircon and ilmenite, consistent with coastal sand from Egypt.

The compositional results obtained from the unknown archaeological glass fragments using μ-XRF align closely with those reported in the study by Zanini et al. [31], which investigated the raw materials used in glass production in the Aquileia area and provided evidence for both primary glass working and recycling practices.

3.4. Sn and Sb data correction

The challenge in investigating SnO_2 and Sb_2O_5 lies in the less accurate characterisation of the exciting beam distribution at high energies, which are necessary to excite Sn and Sb with absorption K-edges at 29.2 keV and 30.49 keV, respectively. Additionally, due to the high energy filtering effect of the polycapillary lens, the K-lines of Sn and Sb are less effectively excited compared to elements with lower atomic number. Their L-lines, in turn, are significantly affected by spectral interferences.

To correct Sn and Sb concentrations, reference materials and LA-ICP-MS data from the archaeological samples were used. The μ-XRF measurements were plotted against the certified values of the reference materials and the corresponding LA-ICP-MS data, and regression equations were calculated to perform the corrections. For the correction process, the corresponding regression equation was used to correct the SnO_2 and Sb_2O_5 concentration of the archaeological samples obtained by μ-XRF and then compared with LA-ICP-MS data. BAM S005—B was not used because the concentrations of Sn and Sb are below the LOQ of μ-XRF and Corning B was excluded for Sn, as its reference concentration falls below the LOQ.

Fig. 4 presents the comparison between μ-XRF and LA-ICP-MS data for SnO_2 and Sb_2O_5, before and after correction, as for the equations, before and after correction, and R coefficients see Table 3. Despite the overall improvement, some archaeological samples still show discrepancies. This may be due to differences in the homogeneity of the glass matrix. The reference materials are compositionally uniform, whereas the archaeological samples often contain micro-scale inhomogeneities. These can lead to local variations in SnO_2 and Sb_2O_5 concentrations depending on the area analysed, particularly given the localised character of μ-XRF analysis at the range of tens of μm.

3.5. Validation of the μ-XRF quantification protocol

For the quantification of the μ-XRF measurements and determination of the concentration of the sample elements, the widely used open source PyMca software suite was properly configured to account for the energy distribution of the exciting beam at the exit of the polycapillary lens [23]. This fundamental parameter-based approach allows for the quantification of elemental concentrations in cultural heritage materials using at least a minimum number of certified materials with similar matrixes with the measured ones to account for unknown instrumental factors (*e.g.* incident flux, solid angle of detection *etc.*). However, the availability of a broader set of certified materials including trace element concentrations spanning an order of magnitude can significantly improve the performance of PyMca, as it has been clearly demonstrated in [32].

This μ-XRF quantification protocol was here successfully validated by LA-ICP-MS, providing a practical foundation for μ-XRF-based quantification. To evaluate the data and make a comparison, the

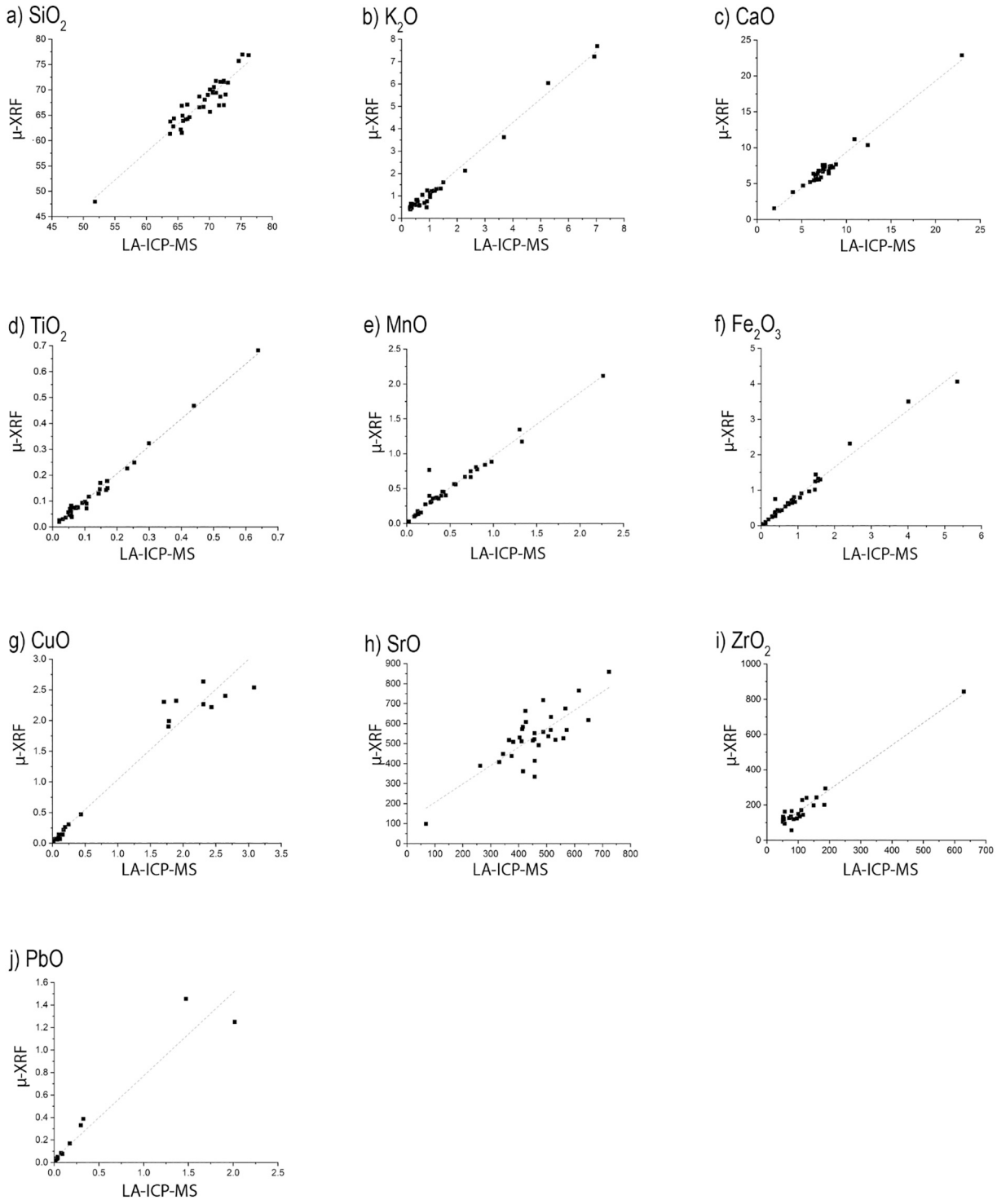

Fig. 3. Scatterplots of μ-XRF data with LA-ICP-MS concentrations of archaeological glass. All the concentration are expressed in wt% except for SrO and ZrO_2 that are expressed in ppm.

concentrations of the elements (expressed in oxides wt% and ppm) of the archaeological glass obtained by the two techniques were compared, to ensure that only the same elements detectable would be considered. Further corrections were applied only for Sn and Sb since μ-XRF is less sensitive to these elements. Consequently, their quantification is more challenging and requires careful calibration and correction methods.

As previously mentioned, the main practical limitation in analysing ancient glass with a μ-XRF is its impracticality in detecting light elements without adding a helium atmosphere in the detection channel. The role of light elements is fundamental for investigating glass composition because they are indicative of the flux and stabilisers used and studying the historical period and geographical location of the production centres and furnaces. In addition, Al_2O_3 also provides information about the provenience of the sand, and based on its concentration into the glass composition, it is possible to discriminate Egypt from Levantine provenance [33]. As for the evidence of recycling, the simultaneous presence of the decolorising agents MnO and Sb_2O_5 at concentrations exceeding their natural upper limits [27,33–36] provides

Table 6
Linear regression equation and the coefficient of determination (R) for major, minor and trace elements of the respective scatterplots in Fig. 2. ACR stands for Applicability Concentration Range, and all the concentration shown in the ACR column are expressed in wt% except for SrO and ZrO_2 that are expressed in ppm.

	$y = a + bx$					
	a	σ_a	b	σ_b	R	ACR
SiO_2	−9.8	4.2	1.12	0.06	0.95	48–77
K_2O	0.05	0.04	1.06	0.02	0.99	0.3–7.8
CaO	−0.6	0.2	0.99	0.03	0.99	1.5–23
TiO_2	−0.006	0.003	1.06	0.02	0.99	0–0.7
MnO	0.04	0.01	0.92	0.02	0.99	0–2.3
Fe_2O_3	0.02	0.02	0.81	0.02	0.99	0–5.5
CuO	0.03	0.04	0.99	0.03	0.98	0–3
SrO	0.003	0.003	1.09	0.07	0.81	70–860
ZrO_2	0.0018	0.0006	1.34	0.05	0.97	50–850
SnO_2	0.0008	0.0148	0.8	0.2	0.73	0.1–0.3
SnO_2_corrected	0.0012	0.0204	1.1	0.2	0.73	0.1–0.3
Sb_2O_5	0.01	0.06	0.5	0.1	0.96	0–2.9
Sb_2O_5_corrected	0.004	0.097	0.9	0.2	0.96	0–2.9
PbO	0.017	0.014	0.75	0.03	0.97	0–2

strong evidence, because these agents are rarely found together in raw glass from primary furnaces. Furthermore, the elevated levels of impurities such as Cu, Co, Sn, and Pb indicate recycling, as their natural oxide concentrations are generally below 100 ppm [1,37], unless intentionally added for purposes such as colouring, decolorising, or opacifying.

A more important distinction is related to the ability of LA-ICP-MS to remove superficial layers from the sample prior to analysis with a pre-ablation, while with μ-XRF it is possible mechanically. By removing these superficial layers, LA-ICP-MS ensures that the analysis is more representative of the bulk composition of the material. This advantage is particularly relevant when considering the influence of surface contamination or alteration layers on the results, and for depth-specific compositional analysis or resolving fine inclusions. By ablating a small portion of the sample with a laser, LA-ICP-MS achieves extremely low detection limits, often in the ppm or ppb range, allowing for precise quantification of most elements [13,38,39]. μ-XRF, however, excels in detecting heavy elements with high atomic number due to their strong fluorescence signals [40,41].

The in-depth elemental information in μ-XRF analysis is constrained by each element's fluorescence energy and the attenuation caused by the glass matrix, which is dependent on the sample matrix composition, density, irradiation geometry and energy distribution of the exciting radiation. Low-energy elements, such as Si, emit X-rays that are absorbed close to the surface, limiting their information depth to just a few μm. In contrast, high-energy fluorescence lines, such as the Sn—K and Sb—K X-rays can emanate from depths of hundreds of micrometres.

In this work, the focus was on validating the acquisition of compositional data from ancient glass. However, μ-XRF had also been employed by [42] to assess alteration states and to monitor corrosion processes in museum glass collections. The analytical validation presented here further demonstrates that μ-XRF is a reliable and robust tool, not only for compositional studies but also for preventive conservation in museums.

4. Conclusion

This study aimed to demonstrate that μ-XRF, despite its known limitations in detecting light elements during field applications, can serve as a highly effective tool for the comprehensive characterisation of glass-making technologies and raw materials. Through a comparative analysis of glass reference materials using both μ-XRF and LA-ICP-MS, it was shown that μ-XRF delivers precise and reliable data for most elements, with LA-ICP-MS providing a robust benchmark for validating its quantitative accuracy. While some discrepancies were observed for certain elements, such as SnO_2 and Sb_2O_5, due to calibration limitations and sample heterogeneity, μ-XRF has proven to be highly effective in detecting and quantifying minor and trace elements, including colouring and impurities in raw materials, which are critical and valuable for provenience studies.

By streamlining the analytical process, μ-XRF facilitates the acquisition of valuable archaeological information, enabling the preliminary identification of raw materials and potential provenience indicators. This can be achieved before resorting to more resource-intensive techniques, thus optimising the analytical workflow and supporting more targeted research strategies. Furthermore, this validation extends its applicability beyond compositional studies by providing critical information for conservation decision-making. This integrated approach enhances both conservation and heritage management, allowing curators and conservators to make informed interventions while minimising the need for destructive sampling.

Looking ahead, the integration of μ-XRF into standardised analytical protocols has the potential to redefine best practices in archaeological science, fostering greater accessibility, repeatability, and interdisciplinarity in the study of ancient glass.

CRediT authorship contribution statement

Sabrina Molinaro: Writing – original draft, Methodology, Investigation, Formal analysis, Data curation, Conceptualization. **Roberta Zanini:** Writing – review & editing, Validation, Supervision,

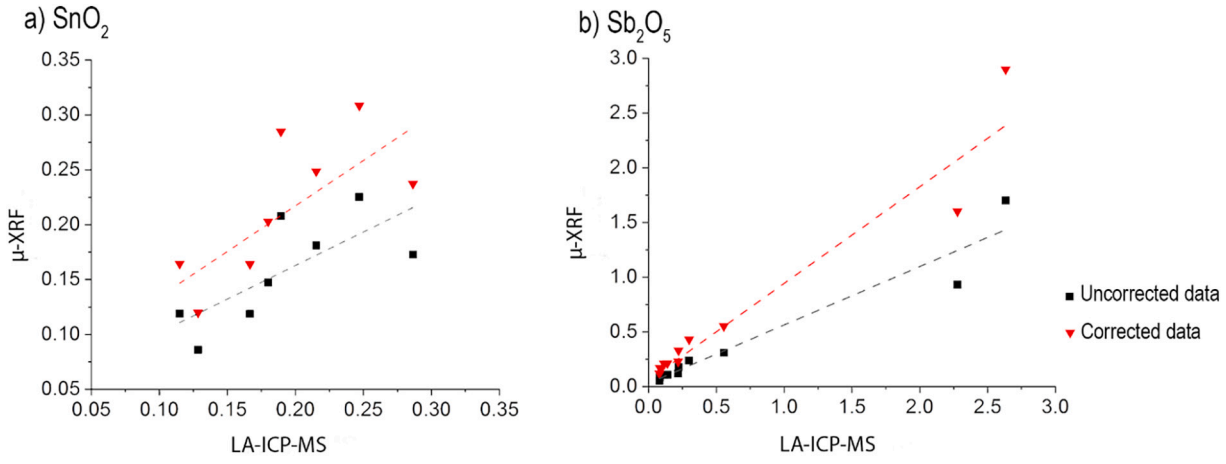

Fig. 4. Scatterplots of μ-XRF data with LA-ICP-MS concentrations of archaeological glass (expressed in wt%) showing (a) SnO_2 and (b) Sb_2O_5 before and after data correction.

Methodology, Investigation, Formal analysis, Data curation, Conceptualization. **Kalliopi Tsampa:** Writing – review & editing, Visualization, Supervision. **Elti Cattaruzza:** Writing – review & editing, Validation, Supervision. **Andreas G. Karydas:** Writing – review & editing, Validation, Supervision, Methodology, Investigation, Funding acquisition, Data curation. **Arianna Traviglia:** Writing – review & editing, Validation, Supervision, Project administration, Funding acquisition.

Declaration of competing interest

The authors declare that they have no known competing financial interests or personal relationships that could have appeared to influence the work reported in this paper.

Appendix A. Supplementary data

Supplementary data to this article can be found online at https://doi.org/10.1016/j.sab.2025.107449.

Data availability

Data will be made available on request.

References

[1] D. Brems, P. Degryse, Trace element analysis in provenancing Roman glass-making, Archaeometry 56 (2014) 116–136, https://doi.org/10.1111/arcm.12063.

[2] K.H.A. Janssens, Modern Methods for Analysing Archaeological and Historical Glass, 1st ed., John Wiley & Sons, Incorporated, Newark, 2013.

[3] T. Trejos, R. Koons, S. Becker, T. Berman, J. Buscaglia, M. Duecking, T. Eckert-Lumsdon, T. Ernst, C. Hanlon, A. Heydon, K. Mooney, R. Nelson, K. Olsson, C. Palenik, E.C. Pollock, D. Rudell, S. Ryland, A. Tarifa, M. Valadez, P. Weis, J. Almirall, Cross-validation and evaluation of the performance of methods for the elemental analysis of forensic glass by μ-XRF, ICP-MS, and LA-ICP-MS, Anal. Bioanal. Chem. 405 (2013) 5393–5409, https://doi.org/10.1007/s00216-013-6978-y.

[4] T. Trejos, R. Koons, P. Weis, S. Becker, T. Berman, C. Dalpe, M. Duecking, J. Buscaglia, T. Eckert-Lumsdon, T. Ernst, C. Hanlon, A. Heydon, K. Mooney, R. Nelson, K. Olsson, E. Schenk, C. Palenik, E.C. Pollock, D. Rudell, S. Ryland, A. Tarifa, M. Valadez, A. Van Es, V. Zdanowicz, J. Almirall, Forensic analysis of glass by μ-XRF, SN-ICP-MS, LA-ICP-MS and LA-ICP-OES: evaluation of the performance of different criteria for comparing elemental composition, J. Anal. At. Spectrom. 28 (2013) 1270, https://doi.org/10.1039/c3ja50128k.

[5] S.-Y. Cheng, Y.-F. Chen, Huang C-CJ, Forensic Applications of Portable X-ray Fluorescence Spectrometer: Glass Samples, 2015.

[6] B.W. Kammrath, A.C. Koutrakos, M.E. McMahon, J.A. Reffner, The forensic analysis of glass evidence: Past, present, and future, in: E. Katz, J. Halámek (Eds.), Forensic Science, 1st ed., Wiley, 2016, pp. 299–336.

[7] R. Corzo, T. Ernst, J. Insana, C. Martinez-Lopez, J. Webb, E. Haase, P. Weis, T. Trejos, Evaluation of the performance of modern X-ray fluorescence spectrometry systems for the forensic analysis of glass, Forensic Chem. 31 (2022) 100447, https://doi.org/10.1016/j.forc.2022.100447.

[8] R.V. Grieken, A. Markowicz, Handbook of X-Ray Spectrometry, 2nd ed., CRC Press, Boca Raton, 2001.

[9] S. Flude, M. Haschke, M. Storey, Application of benchtop micro-XRF to geological materials, Mineral. Mag. 81 (2017) 923–948, https://doi.org/10.1180/minmag.2016.080.150.

[10] H.M. Spencer, K.R. Murdoch, J. Buckman, A.M. Forster, C.J. Kennedy, Compositional analysis by p-XRF and SEM–EDX of medieval window glass from Elgin cathedral, northern Scotland, Archaeometry 60 (2018) 1018–1035, https://doi.org/10.1111/arcm.12357.

[11] A. Oikonomou, P. Triantafyllidis, An archaeometric study of archaic glass from Rhodes, Greece: technological and provenance issues, J. Archaeol. Sci. Rep. 22 (2018) 493–505, https://doi.org/10.1016/j.jasrep.2018.08.004.

[12] M. Haschke, Laboratory Micro-X-Ray Fluorescence Spectroscopy: Instrumentation and Applications, Springer International Publishing, 2014.

[13] B. Wagner, A. Nowak, E. Bulska, K. Hametner, D. Günther, Critical assessment of the elemental composition of corning archeological reference glasses by LA-ICP-MS, Anal. Bioanal. Chem. 402 (2012) 1667–1677, https://doi.org/10.1007/s00216-011-5597-8.

[14] O. Yatsuk, L. Koch, L.C. Giannossa, A. Mangone, G. Fiocco, M. Malagodi, A. Gorghinian, M. Ferretti, P. Davit, C. Iaia, M. Gulmini, Back to black: analysis of the earliest natron glass found in Italy, J. Archaeol. Sci. Rep. 57 (2024) 104648, https://doi.org/10.1016/j.jasrep.2024.104648.

[15] L. Dussubieux, M. Golitko, B. Gratuze, Recent Advances in Laser Ablation ICP-MS for Archaeology, Springer, Berlin Heidelberg, Berlin, Heidelberg, 2016.

[16] S. Cagno, K. Hellemans, K. Janssens, The role of LA-ICP-MS in the investigation of archaeological glass, in: L. Dussubieux, M. Golitko, B. Gratuze (Eds.), Recent Advances in Laser Ablation ICP-MS for Archaeology, Springer, Berlin Heidelberg, Berlin, Heidelberg, 2016, pp. 163–178.

[17] V. Kantarelou, A.G. Karydas, A simple calibration procedure of polycapillary based portable micro-XRF spectrometers for reliable quantitative analysis of cultural heritage materials, X-Ray Spectrom. 45 (2016) 85–91, https://doi.org/10.1002/xrs.2661.

[18] J.T. Van Elteren, N.H. Tennent, V.S. Šelih, Multi-element quantification of ancient/historic glasses by laser ablation inductively coupled plasma mass spectrometry using sum normalization calibration, Anal. Chim. Acta 644 (2009) 1–9, https://doi.org/10.1016/j.aca.2009.04.025.

[19] S.M. Eggins, L.P.J. Kinsley, J.M.G. Shelley, Deposition and element fractionation processes during atmospheric pressure laser sampling for analysis by ICP-MS, Appl. Surf. Sci. 127–129 (1998) 278–286, https://doi.org/10.1016/S0169-4332(97)00643-0.

[20] M. Guillong, D. Günther, Effect of particle size distribution on ICP-induced elemental fractionation in laser ablation-inductively coupled plasma-mass spectrometry, J. Anal. At. Spectrom. 17 (2002) 831–837, https://doi.org/10.1039/B202988J.

[21] J. Henderson, Ancient Glass: An Interdisciplinary Exploration, 1st ed., Cambridge University Press, 2013.

[22] L. Medeghini, M. Botticelli, A.C. Cadena-Irizar, B. Lepri, A.F. Ferrandes, M. Costa, P. Barrulas, Blue shadows of Roman glass artefacts, Microchem. J. 179 (2022) 107526, https://doi.org/10.1016/j.microc.2022.107526.

[23] R. Arletti, S. Quartieri, I.C. Freestone, A XANES study of chromophores in archaeological glass, Appl. Phys. A Mater. Sci. Process. 111 (2013) 99–108, https://doi.org/10.1007/s00339-012-7341-4.

[24] C.M. Jackson, S. Cottam, 'A green thought in a green shade'; compositional and typological observations concerning the production of emerald green glass vessels in the 1st century a.D, J. Archaeol. Sci. 61 (2015) 139–148, https://doi.org/10.1016/j.jas.2015.05.004.

[25] G. Molina, G.P. Odin, T. Pradell, A.J. Shortland, M.S. Tite, Production technology and replication of lead antimonate yellow glass from new kingdom Egypt and the Roman empire, J. Archaeol. Sci. 41 (2014) 171–184, https://doi.org/10.1016/j.jas.2013.07.030.

[26] M. Tite, T. Pradell, A. Shortland, Discovery, production and use of tin-based opacifiers in glasses, enamels and glazes from the late Iron age onwards: a reassessment, Archaeometry 50 (1) (2008) 67–84, https://doi.org/10.1111/j.1475-4754.2007.00339.x.

[27] S. Paynter, C. Jackson, Clarity and brilliance: antimony in colourless natron glass explored using Roman glass found in Britain, Archaeol, Anthropol. Sci. 11 (2019) 1533–1551, https://doi.org/10.1007/s12520-017-0591-5.

[28] P. Degryse, Glass Making in the Greco-Roman World: Results of the ARCHGLASS Project, Leuven University Press, Leuven, Belgium, 2014.

[29] H. Walder, L. Dussubieux, 17 elemental composition of glass beads from the eastern Mediterranean region: Chronology and provenance of material from Tel Anafa, Israel, in: The Elemental Analysis of Glass Beads: Technology, Chronology and Exchange, Leuven University Press, 2022, pp. 347–364.

[30] A.-I. Bidegaray, P. Cosyns, B. Gratuze, H. Terryn, S. Godet, K. Nys, A. Ceglia, On the making, mixing and trading of glass from the Roman military fort at Oudenburg (Belgium), Archaeol. Anthropol. Sci. 11 (2019), https://doi.org/10.1007/s12520-018-0680-0.

[31] R. Zanini, G. Moro, E.F. Orsega, S. Panighello, V.S. Šelih, R. Jaćimović, J.T. Van Elteren, L. Mandruzzato, L.M. Moretto, A. Traviglia, Insights into the secondary glass production in Roman Aquileia: a preliminary study, J. Archaeol. Sci. Rep. 50 (2023) 104067, https://doi.org/10.1016/j.jasrep.2023.104067.

[32] A. Heginbotham, J. Bassett, D. Bourgarit, C. Eveleigh, L. Glinsman, D. Hook, D. Smith, R.J. Speakman, A. Shugar, R. Van Langh, The copper CHARM set: a new set of certified reference materials for the standardization of quantitative X-ray fluorescence analysis of heritage copper alloys*: the copper CHARM set, Archaeometry 57 (2015) 856–868, https://doi.org/10.1111/arcm.12117.

[33] R. Balvanović, Roman and late antique glass in the Mediterranean area and Serbia: its production, compositional types and provenance, Arheologija i prirodne nauke 18 (2022) 127–144, https://doi.org/10.18485/arhe_apn.2022.18.10.

[34] M.J. Baxter, H.E.M. Cool, C.M. Jackson, Further s in the compositional variability of colourless Romano-British vessel glass, Archaeometry 47 (1) (2005) 47–68, https://doi.org/10.1111/j.1475-4754.2005.00187.x.

[35] C.M. Jackson, Making Colourless glass in the Roman period, Archaeometry 47 (2005) 763–780, https://doi.org/10.1111/j.1475-4754.2005.00231.x.

[36] N. Schibille, A. Sterrett-Krause, I.C. Freestone, Glass groups, glass supply and recycling in late Roman Carthage, Archaeol. Anthropol. Sci. 9 (2017) 1223–1241, https://doi.org/10.1007/s12520-016-0316-1.

[37] H.E. Foster, C.M. Jackson, The composition of 'naturally coloured' late Roman vessel glass from Britain and the implications for models of glass production and

supply, J. Archaeol. Sci. 36 (2009) 189–204, https://doi.org/10.1016/j.jas.2008.08.008.

[38] L.W. Adlington, B. Gratuze, N. Schibille, Comparison of pXRF and LA-ICP-MS analysis of lead-rich glass mosaic tesserae, J. Archaeol. Sci. Rep. 34 (2020) 102603, https://doi.org/10.1016/j.jasrep.2020.102603.

[39] T. Trejos, S. Montero, J.R. Almirall, Analysis and comparison of glass fragments by laser ablation inductively coupled plasma mass spectrometry (LA-ICP-MS) and ICP-MS, Anal. Bioanal. Chem. 376 (2003) 1255–1264, https://doi.org/10.1007/s00216-003-1968-0.

[40] S. Bichlmeier, K. Janssens, J. Heckel, P. Hoffmann, H.M. Ortner, Comparative material characterization of historical and industrial samples by using a compact micro-XRF spectrometer, X-Ray Spectrom. 31 (2002) 87–91, https://doi.org/10.1002/xrs.563.

[41] D. Papadopoulou, G. Zachariadis, A. Anthemidis, N. Tsirliganis, J. Stratis, Development and optimisation of a portable micro-XRF method for in situ multi-element analysis of ancient ceramics, Talanta 68 (2006) 1692–1699, https://doi.org/10.1016/j.talanta.2005.08.051.

[42] R. Zanini, V. Risdonne, F. Abate, L.N. Melita, R. Liefkes, L. Burgio, A. Traviglia, Assessing glass alteration on-site: exploring the advantages and limitations of handheld XRF spectrometry, Collect. Curat. (2025), https://doi.org/10.1108/CC-01-2025-0004.